A Bio-Inspired Hybrid Flapping Wing Rotor for High-Efficiency Micro Rotorcraft

Xun Huang, Linghai Lu, and James Whidborne
Cranfield University, Bedfordshire, UK

Marilena Pavel
Delft University of Technology, The Netherlands

ABSTRACT

Enhancing rotor efficiency has been a persistent challenge in the development of micro aerial vehicles (MAV), especially for surveillance and covert operations. This study introduces a new Hybrid Flapping Wing Rotor (Hybrid FWR) configuration inspired by insect wing flapping mechanics to address the efficiency limitation of traditional rotor designs. Unlike traditional rotary systems that rely solely on rotational motion, the Hybrid FWR combines rotational and flapping motions to significantly enhance lift generation. A comprehensive mathematical model was developed to analyse and predict the optimal aerodynamic performance, demonstrating that the Hybrid FWR configuration achieves a substantial improvement, with a power efficiency increase of up to 2.148-fold compared to conventional micro rotorcraft. Experimental validation was conducted to confirm the theoretical predictions, identifying an optimal hybrid ratio of approximately 0.7, which effectively minimises aerodynamic resistance during the upstroke phase while maximising lift during the downstroke. This bio-inspired hybrid approach addresses critical limitations of existing MAV rotors, such as limited operational endurance and range. The findings of this research contribute significantly to the advancement of micro rotorcraft technology, presenting a promising direction for future MAV developments with enhanced flight performance and energy efficiency.

1. NOTATION

Symbols

$\boldsymbol{a_*}$	Effective angle of attack (deg)
$\boldsymbol{A_{flap}}$	Distance travelled by the rotor blade during flapping (m)
$\boldsymbol{AoA}$	Angle of attack(deg)
$\boldsymbol{C_D, C_L}$	Drag and Lift coefficients
$\boldsymbol{C_X, \overline{C_X}}$	Force and average force coefficients along x_{bl} axis, respectively
$\boldsymbol{C_{X,down}, C_{X,up}}$	Force coefficients along x_{bl} axis during downstroke and upstroke, respectively
$\boldsymbol{\overline{C_{d,down}}, \overline{C_{d,up}}}$	Force coefficients are parallel to the chord during downstroke and upstroke, respectively.
$\boldsymbol{C_Z, \overline{C_Z}}$	Force and (average) force coefficients along z_{bl} axis, respectively
$\boldsymbol{C_{Z,down}, C_{Z,up}}$	Force coefficients along z_{bl} axis during downstroke and upstroke, respectively
$\boldsymbol{\overline{C_{L,down}}, \overline{C_{L,up}},}$	Force coefficients perpendicular to the chord during downstroke and upstroke, respectively
$\boldsymbol{I}$	Motor current (A)
$\boldsymbol{k}$	Proportion of the "stepping phenomenon" within the cycle
$\boldsymbol{L_{exp}}$	Experimental lift value (g)

n	Number of sampling points used within each stroke phase
P_{flap_motor}	Power of the flapping motor (W)
P_{rot}	Rotating motor power (W)
P_{rot_motor}	Power of the rotation motor (W)
P_{total}	Total power for the hybrid FWR configuration (W)
r	Current position of the blade element along the rotor's span (m)
St	Strouhal number
T_p	Total duration of the beating cycle (s)
T_{down}, T_{up}	Proportion of downstroke and upstroke periods to the total cycle duration, respectively
Thr	Duty cycle percentage of the PWM wave from the electronic speed controller.
Thr_{flap}	Throttle percentage for the flapping motor
Thr_{rot}	Throttle percentage for the rotation motor
U	Motor voltage (V)
V_{rot}	Rotational linear velocity (m/s)
$V_{\infty hub(x,y,z)}$	Inflow velocities along *x*, *y*, and *z* directions (m/s)
W_x, W_y, W_z	Lateral, spanwise and vertical velocities of the blade element (m/s)
β_{AMP}	Amplitude of the flapping motion (deg)
$\Delta T_{down}, \Delta T_{up}$	Proportion of the "stepping phenomenon" within the downstroke and upstroke durations, respectively
ε	Power efficiency(g/w)
μ	Proportion of upstroke to the entire event cycle length
Ψ	Azimuth angle of the blade element (deg)
φ_{AMP}	Amplitude of the pitching angle (deg)
ϑ	Hybrid ratio

2. INTRODUCTION

Micro Air Vehicles (MAVs), typically defined as aerial platforms featuring a wingspan or rotor diameter within the 15–30 cm range (Figure 1), have attracted extensive research interest owing to their potential in a wide array of applications, such as battlefield reconnaissance, confined-area search and rescue, infrastructure inspection, environmental monitoring, and disaster relief operations[1–5]. Among the various configurations of MAVs[6], rotorcraft-based designs are widely regarded as one of the most favoured and practical subclasses [7].

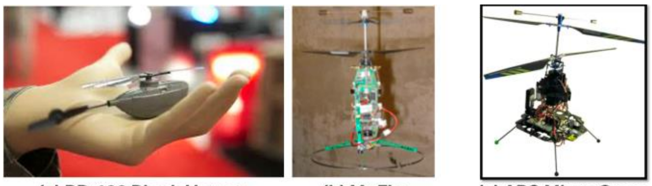

(a) PD-100 Black Hornet (b) MuFly (c) ARS Micro Coax

Figure 1: Typical rotorcraft-based MAV configurations[8][9]

Extending the flight performance of rotorcraft MAVs remains one of the most pressing challenges in the field of unmanned aerial systems (UAVs). Unlike conventional rotorcraft UAVs, these miniature platforms demand significantly different design considerations, as illustrated by the six representative configurations in Table 1.

Traditional rotorcraft UAVs (e.g., ETH CoaX and Yamaha in Table 1), regardless of the substantial size gap, are generally optimised for substantial payload capacity and extended range, with insufficient consideration for the unique demands of light weight, compactness, and endurance that rotorcraft MAVs require. Consequently, such designs often face pronounced challenges in enhancing efficiency. By contrast, rotorcraft MAVs must address four closely interrelated constraints—size, weight, power efficiency, and acoustic emissions [7]. First, their compact geometry, commonly below 30 cm in length, compels engineers to integrate essential electronics and batteries within extremely limited spaces. Second, the necessity for minimal structural mass requires thin, streamlined components capable of supporting stable flight. Third, high power efficiency is imperative for achieving mission durations longer than 10 minutes, given the limited capacity of onboard batteries [7]. Finally, demands for stealth operations impose stringent constraints on noise levels. Together, these four factors must be carefully balanced to advance the payload capability, range and endurance of rotorcraft MAVs.

Table 1: Comparison between representative rotorcraft MAV and UAV configurations

Name		Architecture	Weight	Rotor Diameter	Endurance
PD-100 Black Hornet	MAV	Single rotor	~16–18 g	~123 mm	~20–25 min
MuFly	MAV	Coaxial rotor	~30 g	~120 mm	~6 min
ARS Micro Coax	MAV	Coaxial rotor	~80 g	~140 mm	~10 min
ETH CoaX	UAV	Coaxial rotor	~400–460 g	~480 mm	~7-10 min
Yamaha	UAV	Single rotor	~60-65kg	~3.1m	~60-90min

In an effort to address these challenges, the academic and industrial communities have investigated two principal approaches that adapt conventional UAV design practices to rotorcraft MAVs [10,11]:

- Conventional swashplates and linkages are replaced by mechanical elements such as wheels and discs, thereby reducing overall component count and rotor weight.
- The rotor disk area is increased to improve lift efficiency, which in turn raises overall power efficiency and payload capacity.

These strategies have undergone extensive study and have demonstrated favourable outcomes in various MAV designs[12–14]. For example, the Black Hornet PD-100 (Figure 1*a* and Table 1) achieves notable weight reduction by substituting swashplate linkages with rollers shown in Figure 2. Similarly, the ARS Micro-Coax (Figure 1*c*) employs dual 140 mm coaxial rotors, thereby enlarging the rotor disk area to facilitate 10-minute flights at a maximum takeoff weight (MTOW) of 80 g. This configuration improves power efficiency and payload capacity without a substantial increase in overall aircraft size.

Figure 2: Roller-based rotor hub of PD-100

However, despite initial advances in rotorcraft MAV efficiency, significant barriers remain in the pursuit of further gains. The methods discussed previously, while effective within certain limits, are constrained by traditional rotor design philosophies that largely emphasise enlarging the rotor diameter and simplifying structural components. These strategies have now reached a practical plateau and are inadequate for substantially improving power efficiency. Moreover, any further increase in rotor size risks breaching the MAV classification threshold (15–30 cm wingspan or rotor diameter), thus negating the advantages of miniaturisation (see Table 1 for the ETH CoaX&Yamaha).

In response to these challenges, several researchers have explored alternative design avenues aimed at breaking through the limitations of conventional rotorcraft configurations. For example, studies have investigated the use of high-strength composite materials [15–17] and shape-memory alloys [18–20] to reduce structural mass without compromising rigidity, demonstrating the potential for enhanced thrust-to-weight ratios. Others have drawn inspiration from insect wing kinematics to exploit unsteady aerodynamic effects [15–17] at low Reynolds numbers, an approach that promises higher lift generation and lower acoustic emissions. Although these innovations show promise in boosting performance metrics, they often introduce new complexities, such as more intricate manufacturing processes, increased control difficulties, or heightened susceptibility to mechanical fatigue.

Building upon these emerging strategies, the current study proposed a semi-biomimetic Hybrid Flapping Wing Rotor (Hybrid FWR) concept in the current study, which is an optimal motion-hybridisation strategy that fuses traditional rotor rotation with insect-inspired flapping. The concept is formulated through the Cranfield team's extensive body of work on FWR studies in the past decades [21–23]. The new design tends to maximise power utilisation by concentrating available power on lift generation under low Reynolds number conditions. Preliminary findings suggest that this hybrid approach can enhance rotor efficiency by a factor of 2.148 when compared to conventional MAV rotor systems. The new design philosophy focuses on embedding the flapping mechanism within the standard rotorcraft layout, enabling the Hybrid FWR to be installed on typical rotorcraft MAV architectures with minimal structural changes. By leveraging existing drive shafts and rotor hubs, the flapping components can operate in parallel with rotational motion, thereby generating additional lift from unsteady aerodynamics[24]. This integration also allows the Hybrid FWR to be scaled and adapted for different payload and endurance requirements while preserving the overall compactness demanded by MAV platforms.

The specific objectives of this research are to:

- Determine the feasibility of the proposed Hybrid FWR model for MAV applications.
- Investigate the existence of an optimal operating mode by combining conventional rotor rotation and flapping motion.
- Analyse whether an optimal mode exists between FWR and rotorcraft, and explain why, focusing on the aerodynamic and energetic mechanisms underlying the hybridisation of these two distinct modes.
- Develop a working prototype to validate both the design concept and theoretical hypotheses regarding its improved aerodynamic performance.

The following procedure in Figure 3 is outlined to validate and analyse the optimal motion-hybridisation strategy for the Hybrid FWR:

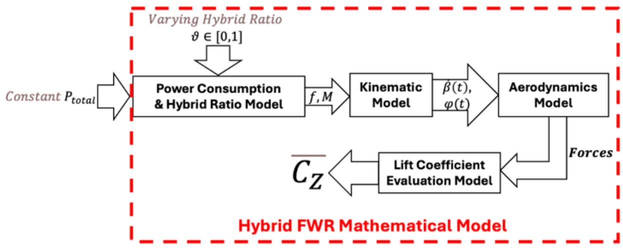

Figure 3: Hybrid FWR optimal motion-hybridisation strategy

First, the Hybrid FWR system's mechanical structure is conducted for the study, followed by the development of its kinematic model, aerodynamic model, power consumption model, and lift coefficient evaluation model. On this basis, a method for evaluating the lift coefficient of various Hybrid FWR operating conditions under a given power level is constructed. In this approach, a fixed total power (P_{total}) is input into the Hybrid FWR mathematical model. Subsequently, a coefficient termed the Hybrid Ratio ϑ, which can alter the flapping and rotational motion-hybridisation strategy, is varied from 0 to 1 in increments of 0.1. This procedure allows the Hybrid FWR to switch among purely rotational mode, purely flapping mode, or a blend of both modes. Such switching affects the flapping frequency and rotational speed of the rotor, thereby influencing the outputs of the kinematic model and, in turn, affecting the aerodynamic model and the predicted average lift coefficient. By applying this method, identifying the Hybrid Ratio that yields the highest lift coefficient at a given power input establishes the optimal motion-hybridisation strategy. A subsequent analysis of the underlying principles of this optimal hybrid strategy, along with experimental validation to confirm its actual existence, would then fulfil the four research objectives above.

This study posits that by striking an optimal balance among size, weight, acoustic emissions, and power efficiency, the Hybrid FWR methodology could provide a promising avenue for advancing the performance of next-generation rotorcraft MAVs. The structure of the paper is outlined below, fulfilling the procedure described in Figure 3. Section 2 will first present and analyse the design features and mechanical structure of the Hybrid FWR concept, explaining how traditional rotor systems “evolve” into Hybrid FWR rotors incorporating bio-inspired motion[25,26]. Section 3 will establish the Hybrid FWR mathematical model, enabling a mathematical description of its power consumption, aerodynamic performance, and wing kinematics to provide the necessary mathematical groundwork for the analysis procedure depicted in Figure 3. Section 4 will formulate a theory regarding the high-power efficiency of the Hybrid FWR based on the analysis results obtained through the procedure shown in Figure 3. Section 5 will describe the experiments conducted to verify the optimal hybrid ratio identified in Section 4, thereby validating the proposed high-power efficiency theory. Finally, the conclusions are drawn in Section 6, summarising the findings and contributions of this study.

3. DESIGN OF THE HYBRID FWR

3.1 Conceptual Design

Figure 4 illustrates how traditional UAV rotors 'evolve' into the Hybrid FWR concept, proposed in the current study, and highlights their differences in active and passive degrees of freedom (DoF). In a conventional rotorcraft UAV, the rotor is directly driven by a rotational motor, thereby providing an active in-plane rotation (Ψ) that generates lift. This design typically employs an active blade pitch angle (φ) for cyclic pitch control while relying on passively induced out-of-plane flap motion governed by aerodynamic forces. By contrast, the Hybrid model derived from the conventional rotorcraft UAV concept—introduces an additional flapping motor shown in Figure 4 (right). Through a system of gears and linkages, the flapping motor actively drives the rotor's flapping motion, resulting in an active flap angle (β) reminiscent of insect or avian flight. Due to spatial limitations in the Hybrid FWR's structure, as illustrated in Figure 4, the new design does not include an active pitch control mechanism. Instead, a pitch (feathering) hinge is incorporated to accommodate dynamically coupled pitch variations arising from flapping, torsional, inertial, and other effects. Hence, φ becomes passive in this new design.

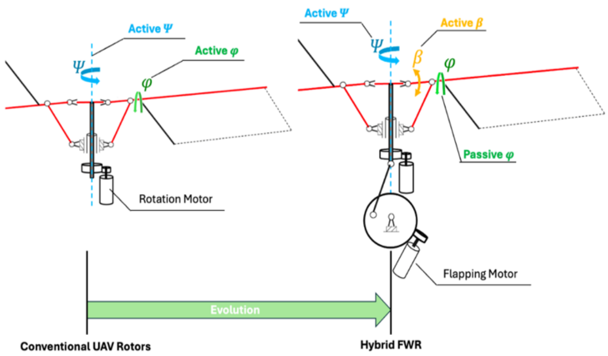

Figure 4: Illustration of design transition from conventional rotors to bio-inspired rotors

3.2 Mechanical Structure & Core Components

The Hybrid FWR MAV prototype fabricated using 3D-printed nylon material in Figure 5 has a height of 100 mm and a base diameter of 25 mm × 25 mm. Beneath the base where the prototype is mounted, a lightweight flight controller weighing only 3 g, along with the battery, is installed on the frame. The flight controller runs the flight control software, while the battery provides power. Furthermore, as illustrated in Figure 6, the maximum mechanical range of β motion extends from $\beta_{min} = -10°$ during the downstroke to $\beta_{max} = 35°$ during the upstroke.

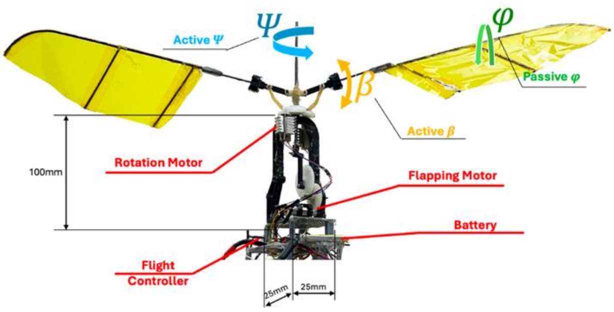

Figure 5: Illustration of the Hybrid FWR test prototype designed in the current study

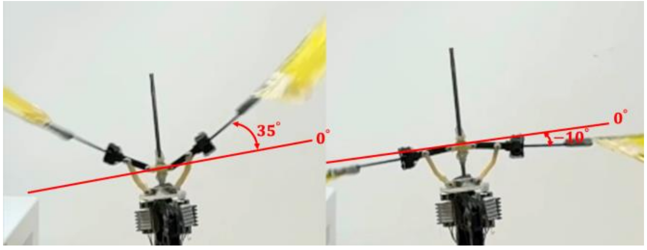

Figure 6 Limitation of flapping angle range (β) (Left – upstroke, Right – downstroke)

A limit-stop mechanism in Figure 7 is employed to ensure φ remains within its permissible physical bounds. By adjusting the position of the limit-stop rod, the motion range of the free-sliding block is constrained, thereby maintaining φ between 10° and 25°. Moreover, repositioning the limit-stop rod enables further refinement of these upper and lower angle limits.

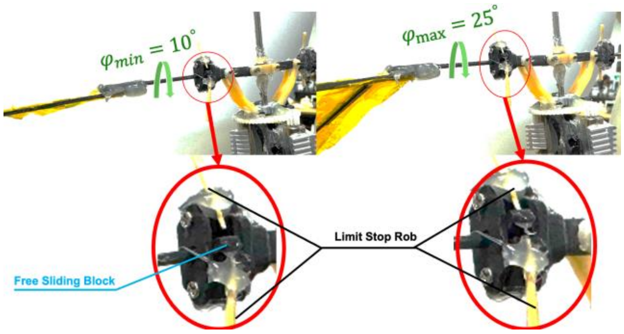

Figure 7: Illustration of pitching angle $\boldsymbol{\varphi}$ limitation

A unique feature that warrants further examination is the rotor's passively governed pitch angle φ. During rotor lift generation, both the rotation motor and the flapping motor are powered simultaneously, enabling active rotation as well as active flapping. Meanwhile, as mentioned above, the passive φ in this new design is determined by the combined influence of aerodynamic and inertial forces. High-speed camera observations in Figure 8 show that φ is primarily driven by the inertial forces from the flapping motion and the aerodynamic forces from the incoming flow, resulting in an asymmetric periodic pattern akin to the asymmetrical wing-pitching motion of dragonflies [27]. Typically, at the onset of the upstroke, φ increases quickly to $\varphi_{max} = 25°$ and remains at this value throughout the stroke, whereas during the downstroke, it decreases rapidly to $\varphi_{min} = 10°$ and stays there. The next section provides a more detailed kinematic model of this passively induced pitching motion stemming from the flapping dynamics.

Figure 8: Hybrid FWR wing motion during one flapping cycle

4. HYBRID FWR MODEL DEVELOPMENT

As outlined in Figure 3, the assessment of an optimal motion-hybridisation strategy necessitates the development of a kinematic model, an aerodynamic model, a power consumption model, and a lift coefficient evaluation model for the Hybrid FWR. This section presents a detailed formulation of these models.

4.1 Kinematics Modelling

The kinematic model serves as the most critical component among all models. Its accuracy directly influences the predictive reliability of the subsequent aerodynamic model. Moreover, its formulation is the most complex aspect of the overall modelling process, as it requires a mathematical description of the passive characteristics of the Hybrid FWR's φ angle and its induced kinematic coupling effects.

As stated in the previous section, the flapping motion of β and the asymmetric periodic kinematics of φ in the Hybrid FWR closely resemble those observed in dragonfly flight. Figure 9(*a*) illustrates the fundamental flight mechanism of a dragonfly. Within the dragonfly's body, each wing is actuated by two muscles arranged in a configuration analogous to a parallel mechanical structure. When both muscle attachment points exert force in the same direction, a flapping motion occurs, actively inducing β changes. Conversely, if the forces applied at the two muscle attachment points differ, a twisting motion is generated, actively modifying φ. Figure 9(*b*) depicts these kinematic variations over a complete flapping cycle of dragonflies, demonstrating that both β and φ are actively controlled by the muscles.

However, although the asymmetric mechanism governing φ in the Hybrid FWR closely resembles that observed in biological dragonflies, significant differences remain between the flapping kinematics of the Hybrid FWR and those of natural dragonfly flight. These differences primarily arise from two factors: <u>mechanical structural limitations</u> and the <u>passive pitching kinematics</u> of φ. The mechanical structural constraints, as discussed earlier, are defined by the limitations on the flapping angles, $\beta_{max} = 35°$ and $\beta_{min} = -10°$, as well as the limitations on the passive pitching angle, $\varphi_{max} = 25°$ and $\varphi_{min} = 10°$. In contrast, the passive pitching kinematics of φ reveal a distinct divergence from dragonfly flight mechanics, which can primarily be attributed to two key aspects:

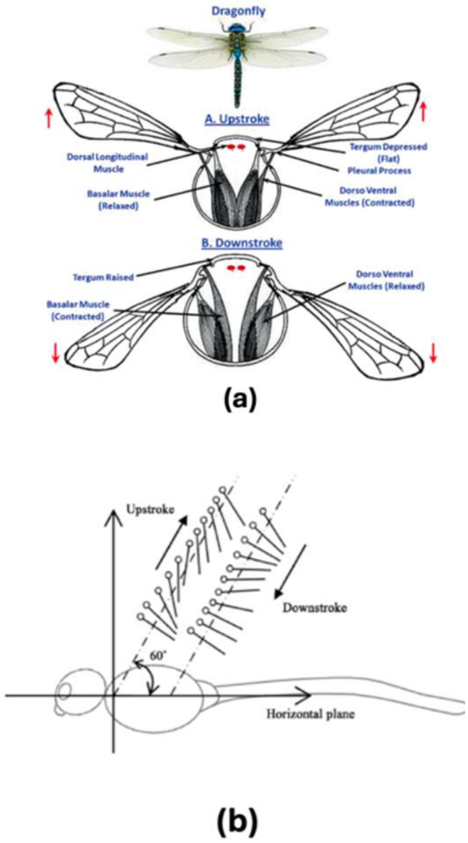

Figure 9: DragonFly flight principle FWR

Firstly, the pitching angle φ of the biological dragonflies[28], is actively regulated by specialised musculature (Figure 9 (*a*)), allowing its precise control over wing flapping. In contrast, in the Hybrid FWR, φ is governed passively by the flapping velocity, primarily driven by the inertial forces of the wings. As a result, the timing for reaching φ_{max} and φ_{min}, as well as the duration of the wing's residence at these extreme positions, vary with changes in flapping velocity. This fundamental difference—active control in dragonflies versus passive, inertia-driven kinematics in the Hybrid FWR, underscores the necessity of considering flapping velocity and acceleration effects when modelling the wing pitching motion of the Hybrid FWR.

Figure 10 summarises high-speed camera observations, illustrates the relationship between flapping velocity $\dot{\beta}$ and the passive pitching angle φ. The blue curve represents the variation in flapping velocity over a single flapping cycle. It demonstrates the changes in wing passive pitching angle, the timing of reaching φ_{max} and φ_{min}, and the duration of the wing's residence at these limitation positions is closely related to the acceleration of the flapping velocity.

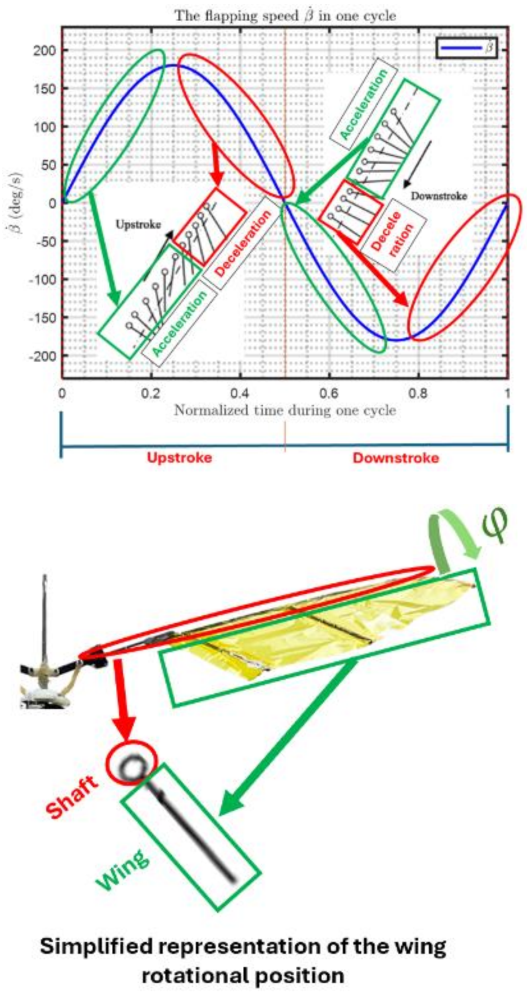

Figure 10: Relationship between flapping speed and wing rotation position

Taking the upstroke as an example, when the flapping velocity is in the acceleration phase, as highlighted by the green oval frame in Figure 10, the inertial forces acting on the wing cause a lag effect, leading to the wing rotating about the pitch hinge (the red shaft) and pitching upwards until it reaches the mechanical constraint at $\varphi_{max} = 25°$ (green square frame, upstroke marked in Figure 10). Conversely, when the flapping velocity enters the deceleration phase, highlighted by the red oval frame (upstroke in Figure 10), the inertial forces induce a lagging downward pitch, causing the wing to move away from $\varphi_{max} = 25°$ and gradually reduce its angle, as indicated by the red rectangular frame.

During the downstroke, the acceleration and inertial forces rapidly bring the wing into contact with the mechanical constraint $\varphi_{min} = 10°$, where it remains until the downstroke velocity begins to decelerate, at which point the wing angle slowly pitches up again (red square frame, downstroke). These passive mechanisms reveal a strong relationship between flapping velocity, acceleration, and pitching angle, as well as the duration and timing of reaching φ_{max} and φ_{min}, underscores the necessity of incorporating these dynamics into the kinematic modelling of the wing to accurately capture the observed behaviours. The phenomenon where the wing becomes temporarily fixed at φ_{max} and φ_{min} during flapping is referred to as the "stepping phenomenon" in this study.

Secondly, the passive pitching characteristics of the Hybrid FWR significantly influence the duration distribution between upstroke and downstroke within a flapping cycle. Experimental observations of the mechanical structure reveal that, under constant motor input power, the proportion of time spent on upstroke and downstroke is strongly affected by the aerodynamic forces acting on the wing. This aligns with engineering principles: when aerodynamic forces on the wing are high, motor loading increases, resulting in lower acceleration under the same power input. Consequently, achieving the same motion requires more time. Conversely, lower aerodynamic forces reduce motor loading, the same power allowing higher acceleration and shorter motion times. In the Hybrid FWR, this effect is particularly pronounced. During the upstroke, the passive pitching-up motion, driven by inertial forces, reduces the effective angle of attack relative to the incoming airflow, leading to lower aerodynamic loads on the motor. In contrast, the downstroke experiences higher aerodynamic loads due to the increased angle of attack. As a result, the upstroke duration is shorter than the downstroke within the flapping cycle.

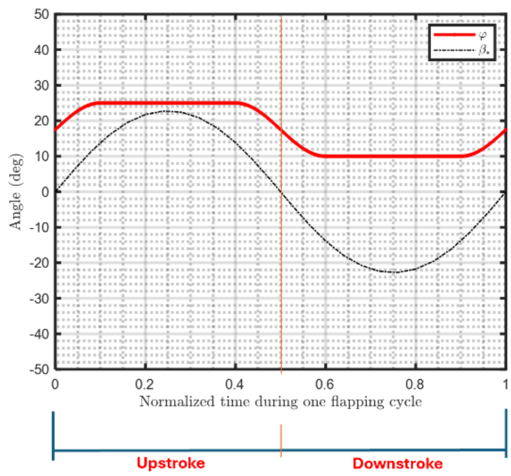

Figure 11: Approximate relationship between the incoming flow angle β_* and the passive pitching angle $\boldsymbol{\varphi}$ of the wing (summarized from high-speed camera observations)

Figure 11 demonstrates the relationship between the inflow angle (β_*), which characterises the direction of the relative inflow velocity acting on the wing, and the corresponding passive pitching angle (φ) of the wing.

The β_* definition and representation is illustrated in Figure 12 and Eq. (1).

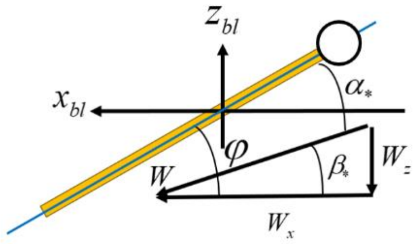

Figure 12: Definition of Hybrid FWR blade element's angles β_*

(1) $$\beta_* = arctan\frac{W_z}{W_x}$$

in which W_z represents the inflow velocity along the vertical blade (wing) element axis (Z_{bl}), which is primarily influenced by the flapping velocity. W_x denotes the inflow velocity along the horizontal blade axis (X_{bl}), which is mainly affected by the blade elements' tangential velocity. The small circular marker on the wing in Figure 12 represents the passive rotational shaft of the wing (corresponding to the structure highlighted by the red frame in Figure 10). Furthermore, as shown in Figure 11, the difference between φ and β_* defines the effective angle of attack a_* for a blade element, expressed below:

(2) $$a_* = \varphi(t) - \beta_*$$

Based on Eq. (2) and the analysis of Figure 10, assume the rotor operates under conditions where the resultant velocity W remains relatively constant. During the upstroke, a_* reduces, resulting in lower aerodynamic loads during the upstroke. Conversely, during the downstroke, the negative β_* produces a much larger a_*, significantly increasing the aerodynamic loads. This discrepancy in aerodynamic loads between the upstroke and downstroke has been observed through high-speed camera analysis of the Hybrid FWR. It was found to have a significant impact on the time distribution of the upstroke within the overall flapping cycle. Figure 13 illustrates the proportion of time spent in the upstroke and downstroke under varying Hybrid Ratios ϑ, which is defined as a combined measure of flapping frequency and rotational speed and will be further detailed in the next Subsection. The results in the figure reveal that under different flapping conditions ($\vartheta = 0.3\ or\ \vartheta = 0.6$), the proportion of time experienced during the upstroke and downstroke differs, leading to variations in aerodynamic loads applied to the upstroke within the total flapping cycle. Moreover, the aerodynamic loads on the wing of both scenarios during the upstroke are consistently lower than those during the downstroke. Consequently, under constant motor power, the upstroke always occupies a shorter duration of the overall flapping cycle compared to the downstroke. This pattern has also been consistently observed in other Hybrid Ratio conditions studied with high-speed camera analysis of the Hybrid FWR.

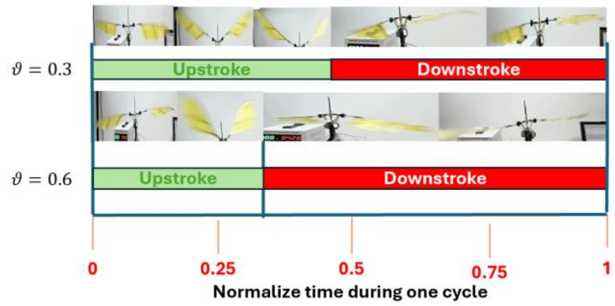

Figure 13: Upstroke time under different flapping conditions

Due to the significant kinematic differences between the Hybrid FWR and dragonflies as described above, the wing kinematic model of the Hybrid FWR cannot be directly adapted from that of dragonflies. Instead, the model should be refined to capture two unique kinematic phenomena observed in the Hybrid FWR:

- Point 1: The duration of the "stepping phenomenon" at φ_{max} and φ_{min}: These durations are strongly influenced by the correlation between flapping velocity and the passive pitching angle φ. Hence, it must be accurately modelled to reflect this dependency.
- Point 2: The proportion of the upstroke duration within the total cycle: As discussed earlier, aerodynamic load asymmetry causes discrepancies in the durations of upstroke and downstroke. This asymmetry can be quantified through the upstroke time proportion within the overall flapping cycle.

Therefore, unlike the flapping kinematics theories for dragonflies presented in the referenced literature [29,30], the Hybrid FWR model introduces two transition time coefficients ΔT_{up} and ΔT_{down} to represent the "stepping phenomenon" durations at φ_{max} and φ_{min}, addressing Point 1. Additionally, the coefficient μ is introduced to represent the proportion of upstroke time within the total cycle, addressing Point 2.

The next step moves on to build the kinematic model, starting with the flapping kinematics of the rotor. The equation governing the flapping velocity is expressed as below,

$$\dot{\beta}(t) = \begin{cases} \pi \cdot \beta_{AMP} \cdot f \cdot \mathbf{sin}\left(\frac{\pi t}{\mu \cdot T}\right) & t < \mu \cdot \\ -\pi \cdot \beta_{AMP} \cdot f \cdot \mathbf{sin}\left[\frac{\pi(t-\mu \cdot T)}{(1-\mu) \cdot T}\right] & t \geq \mu \cdot \end{cases} \tag{3}$$

in which μ represents the proportion of the upstroke duration within the total cycle time T, characterising the kinematic asymmetry of the Hybrid FWR between upstroke and downstroke. $T = \frac{1}{f}$ denotes the one whole cycle duration, where f is the flapping frequency, and β_{AMP} is the flapping amplitude.

By integrating the velocity equation Eq. (3), the flapping dynamics for the Hybrid FWR can be derived, as expressed in Eq. (4):

$$\beta(t) = \begin{cases} \beta_{INIT} - \beta_{AMP} \cdot f \cdot \mu T \cdot \mathbf{cos}\left(\frac{\pi t}{\mu T}\right) & t < \mu T \\ \beta_{INIT} + \beta_{AMP} \cdot f \cdot [(1-\mu) \cdot T]\mathbf{cos}\left[\frac{\pi(t-\mu T)}{(1-\mu) \cdot T}\right] & t \geq \mu T \end{cases} \tag{4}$$

in which β_{INIT} represents the initial flapping angle, according to the mechanical constraints defined in Figure 6, which is set to $10^\circ + \frac{35^\circ}{2} = 27.5^\circ$. β_{AMP} denotes the flapping amplitude, which is constrained by the structure shown in Figure 6 and limited to $\frac{35^\circ}{2} = 17.5^\circ$.

The pitching kinematics of the Hybrid FWR are significantly more complex. Unlike the flapping kinematics, which primarily follows trigonometric characteristics, the pitching motion exhibits the "stepping phenomenon" caused by mechanical constraints at two limiting angles φ_{max} and φ_{min}, as shown in Figure 7 and further illustrated by the red curve in Figure 11. Therefore, in addition to the parameter μ used in the flapping kinematics to describe the time asymmetry between upstroke and downstroke, two new transition time coefficients, ΔT_{up} and ΔT_{down} are introduced to characterise the duration of the "stepping phenomenon" at the mechanical limits. The resulting set of equations for the pitching angle kinematics is formulated as follows:

if *t* belongs $[-\frac{\Delta T}{2}, \frac{\Delta T_{up}}{2}]$, and then:

$$\varphi(t) = \frac{\varphi_{max} + \varphi_{min}}{2} + \frac{\varphi_{max} - \varphi_{min}}{2} sin(\pi \frac{t}{\Delta T_{up}}) \tag{5}$$

if *t* belongs $(\frac{\Delta T_{up}}{2}, T_{up} - \frac{\Delta T_{up}}{2})$, and then:

$$\varphi(t) = \varphi_{max} \tag{6}$$

if t belongs $[T_{up} - \frac{\Delta T_{up}}{2}, T_{up}]$, and then:

$$\varphi(t) = \frac{\varphi_{max} + \varphi_{min}}{2} + \frac{\varphi_{max} - \varphi_{min}}{2} sin(\pi \frac{T_{up} - t}{\Delta T_{up}}) \tag{7}$$

if t belongs $(T_{up}, T_{up} + \frac{\Delta T_{down}}{2}]$, and then:

$$\varphi(t) = \frac{\varphi_{max} + \varphi_{min}}{2} + \frac{\varphi_{min} - \varphi_{max}}{2} sin(\pi \frac{t - T_{up}}{\Delta T_{down}}) \tag{8}$$

if t belongs $(T_{up} + \frac{\Delta T_{down}}{2}, T_p - \frac{\Delta T_{down}}{2})$, and then:

$$\varphi(t) = \varphi_{min} \tag{9}$$

if *t* belongs $[T - \frac{\Delta T_{down}}{2}, T_p]$, and then:

$$\varphi(t) = \frac{\varphi_{max} + \varphi_{min}}{2} + \frac{\varphi_{min} - \varphi_{max}}{2} sin(\pi \frac{T_p - t}{T_{down}}) \tag{10}$$

in which t is the current time during one flapping cycle. $T_p = \frac{1}{f}$ is the period of pitching angle, T_{up} denotes the duration of the upstroke as a proportion of the total cycle, while T_{down} represents the corresponding proportion for the downstroke. Their expressions are defined as follows:

$$\begin{cases} T_{up} = \mu T_p \\ T_{down} = (1-\mu) T_p \end{cases} \tag{11}$$

The transition time coefficients ΔT_{up} and ΔT_{down} describing the "stepping phenomenon" are given by the following expressions:

$$\begin{cases} \Delta T_{up} = (1-k) T_{up} \\ \Delta T_{down} = (1-k) T_{down} \end{cases} \tag{12}$$

in which k represents the proportion of time spent at the stepping phenomenon, relative to the total upstroke or downstroke duration. It is influenced by factors such as flapping velocity, acceleration, mechanical smoothness, and rotational axis damping. In practice, k is highly sensitive to flapping conditions and manufacturing quality, such as the fit tolerance of the bearing, which can significantly affect the motor power. Moreover, given its dependency on these empirical variables, k is almost exclusively determined through experimental observation. Based on repeated high-speed camera analyses of the mechanical structure under various operating conditions, k is set to an average value of 0.9 for the operating range 1-20Hz of our Hybrid FWR.

The kinematic model described above provides a comprehensive representation of the wing kinematics observed during high-speed camera experiments with the Hybrid FWR. Using the equations outlined, the typical kinematic patterns can be derived, as illustrated in Figure 14.

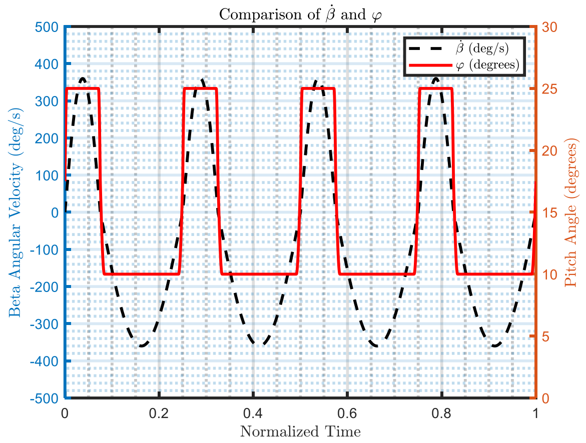

Figure 14: A wing kinematics case of Hybrid FWR

Figure 14 illustrates the wing kinematics of the Hybrid FWR under conditions where $f = 4Hz$, $\mu = 0.3$, and $k = 0.9$. The results shown in the figure align perfectly with the passive wing motion principles depicted in Figure 10. However, it should be noted that this example represents only one of the many complex motion patterns exhibited by the Hybrid FWR. In practice, due to the varying aerodynamic loads on the wing, the parameter μ, dynamically changes in response to these aerodynamic forces. As a result, a dedicated model linking μ to aerodynamic loads is necessary and will be discussed in Section 3.6.

At this stage, the presented equations (Eq. 3–Eq. 12) are sufficient to describe all kinematic phenomena of the Hybrid FWR observed in the experiments. However, these equations often require recalibration in practical applications to account for the condition of the mechanical structure. This is particularly critical for the k value, which must be periodically refined through high-speed camera observations.

4.2 Aerodynamics Modelling

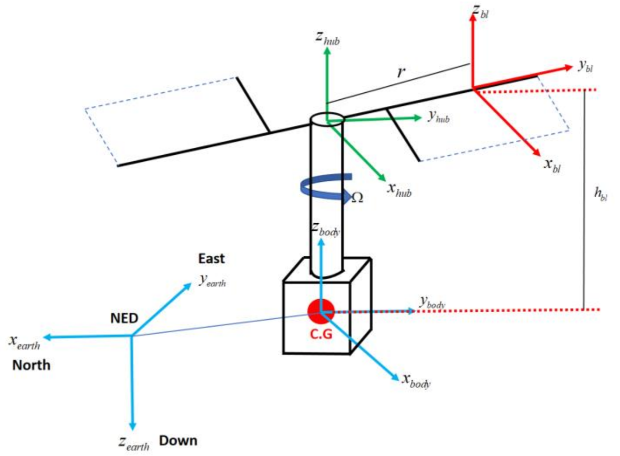

Figure 15: Hybrid FWR Coordinate System Definition

Based on the wing kinematics derived in the previous section, the aerodynamic forces of the Hybrid FWR can be easily determined. This can be achieved by applying Blade Element Theory (BET) [31–33] to calculate the aerodynamic forces on each blade element and then integrating them across the entire wingspan. The inflow velocity components in the wing element coordinate system $x_{bl} - y_{bl} - z_{bl}$ can be calculated using the following equations:

$$\textbf{(13)} \quad \begin{cases} \boldsymbol{W_x(r,t)} = \\ -\boldsymbol{\Omega r \cos[r \cdot \beta(t)] - V_{\infty hub_x} \sin \Psi + V_{\infty hub\_y} \sin(\frac{\pi}{2} - \Psi)} \\ \boldsymbol{W_y(r,t)} = \\ \boldsymbol{[V_{\infty hub_x} \cos \Psi +} \\ \boldsymbol{V_{\infty hub_y} \cos\left(\frac{\pi}{2} - \Psi\right)] \cos[r \cdot \beta(t)]} \\ \boldsymbol{W_z(r,t)} = \\ \boldsymbol{(v_i - V_{\infty hub_z}) \cos[r \cdot \beta(t)] +} \\ \boldsymbol{v_\beta(r,t) + V_{\infty hub\_x} \cos \Psi \sin[r \cdot \beta(t)]} \end{cases}$$

in which W_y denotes the lateral velocity of the blade element. The symbol Ω (in rad/s) indicates the rotor rotational speed, and r corresponds to the blade element position along the wingspan. Ψ defines the azimuth angle of the blade element. The parameters $V_{\infty hub_x}$ and $V_{\infty hub_y}$ define the inflow velocities along x_{bl} and y_{bl} directions of the blade element, respectively, while v_i denotes the induced velocity. The flapping linear velocity at the current blade element position, denoted as $v_\beta(r)$, is expressed by the following equation, which incorporates $V_{\infty hub_z}$, the inflow velocity in the z_{bl} direction.

$$\textbf{(14)} \quad v_\beta(r,t) = -[r \cdot \dot{\beta}(t)]\left(v_i - V_{\infty hub_z}\right) \cos[r\beta(t)]$$

Next, using Eq. (1) and Eq. (2), the inflow angle β^* and the effective angle of attack α^* can be determined. With these two angles, the aerodynamic forces can be calculated. The first step is to transform the aerodynamic coefficients C_L and C_D in the coordinate system of Figure 12, into the $x_{bl} - y_{bl} - z_{bl}$ coordinate system in Figure 15, as described below:

$$\textbf{(15)} \quad \begin{cases} C_z(a_*, \beta_*) = C_L\,(a_*) \cdot cos\,\beta_* - C_D\,(a_*) \cdot sin\,\beta_* \\ C_x(a_*, \beta_*) = C_D(a_*) \cdot cos\,\beta_* + C_L(a_*) \cdot sin\,\beta_* \end{cases}$$

Furthermore, by performing discrete integration across all blade elements along the span, the total lift force $F_{zbl}(a_*, \beta_*, r, t)$ and total drag force $F_{xbl}(a_*, \beta_*, r, t)$ in the $x_{bl} - z_{bl}$ A coordinate system can be obtained:

$$\textbf{(16)} \quad \begin{cases} \boldsymbol{F_{xbl}(a_*, \beta_*, r, t) = \frac{1}{2}\sum C_x(a_*, \beta_*)\rho[W_x{}^2(r,t) + W_z{}^2(r,t} \\ \boldsymbol{F_{zbl}(a_*, \beta_*, r, t) = \frac{1}{2}\sum C_z(a_*, \beta_*)\rho[W_x{}^2(r,t) + W_z{}^2(r,t} \end{cases}$$

It is important to note that the above equations represent only the most fundamental lift and drag models for the Hybrid FWR. In practice, the key to constructing accurate lift and drag models lies in developing precise $C_L\,(a_*)$ and $C_D\,(a_*)$ models specifically tailored for micro, highly flexible rotors like the Hybrid FWR. This is because its wings exhibit high flexibility, operate in a low Reynolds number regime [34], and experience large a_* due to flapping. These characteristics render traditional steady-state $C_L\,(a_*)$ and $C_D\,(a_*)$ models inadequate [35][23] [36–38]. Previous research by the authors has demonstrated that employing a physically driven digital twin is essential to obtaining reliable $C_L\,(a_*)$ and $C_D\,(a_*)$ models for such micro flexible rotors. Detailed methodologies for this approach are provided in the authors' earlier work [39]. Since high-fidelity aerodynamics model development is not the primary focus of this study, the equations provided above are sufficient to address the research questions discussed in the subsequent sections.

4.3 Power Consumption Modelling Based on Hybrid Ratio Variation

Furthermore, it is necessary to develop a model for power consumption and hybridisation ratio, as illustrated in Figure 3. This model is essential for assessing the efficiency of the Hybrid FWR. This model is critical for evaluating its efficiency under various flapping-rotation hybrid conditions.

As highlighted in the Introduction, the primary design objective of the study is to enhance flight efficiency. Whether developing fixed-wing aircraft or rotorcraft, the primary approach to improving flight efficiency typically involves increasing the lift-to-drag ratio. Fundamentally, this concept translates to generating as much lift as possible for the same power consumption. In other words, under constant flight conditions, the goal is to achieve the highest possible lift coefficient while maintaining the same power input. The two key factors in this optimization are power and lift coefficient. Therefore, the first step in analyzing the efficiency optimisation of the Hybrid FWR is to establish its power model.

As shown in Figure 3, the power system of the Hybrid FWR consists of two identical 8520 coreless motors, with specifications listed in Table 3.

Table 2: 8520 coreless motors

Diameter	8.6 mm
Length	19.5 mm
Weight	5.9 g
Maximum voltage	4.2 V
Maximum speed	60000 RPM

If the Pulse Width Modulation (PWM) duty-cycle percentage ($Thr(\%)$, ranging from 0% to 100%) of the electronic speed controller on the Hybrid FWR's flight control system is used as the input parameter for motor system power control, the relationships between Thr, motor voltage, current, and power have been experimentally fitted as follows:

$$\textbf{(17)} \quad \begin{cases} I = 0.08811 \times \cdot Thr + 0.5217 \\ U = 0.02817 \times \cdot Thr + 0.1742 \\ P = IU \end{cases}$$

Here, I represents the motor current (in amperes), U denotes the motor voltage (in volts), and P represents the input power of a single motor (in watts). The power of the flapping motor (Figure 4) is designated as P_{flap}, while the power of the rotational motor (Figure 5) is denoted as P_{rot}. The total power consumption of the Hybrid FWR system, P_{total}, is defined as the sum of these two components: $P_{total} = P_{rot} + P_{flap}$. P_{total} represents the overall power required by the Hybrid FWR system.

Further experimental tests were conducted to establish the relationship between the PWM duty cycle input Thr and the torque output of the rotational motor, as well as the relationship between Thr and the flapping frequency of the flapping motor, as expressed in Eq. (18). Here, f is the flapping frequency (in Hz) and M is the torque (in Nm). With these parameters, the motor power can be mathematically linked to the wing kinematics, enabling a comprehensive integration of the power model in Eqs. (17) and (18) and the kinematics characteristics from Eqs.(3) to (12) of the Hybrid FWR.

$$\textbf{(18)} \qquad \begin{cases} f = 0.2 \times \cdot Thr + 3.386 \times 10^{-16} \\ M = 0.00143 \times Thr + 0.000108 \end{cases}$$

In the Hybrid FWR motor control flight program, the power distribution between the flapping motor and the rotational motor is determined by a parameter referred to as the "Hybrid Ratio." For clarity, the Hybrid Ratio, along with the PWM duty cycle inputs for these two motors, are denoted as Thr_{rot} and Thr_{flap}, respectively. Their relationship with the Hybrid Ratio is expressed as follows:

$$\textbf{(19)} \qquad \begin{cases} Thr_{flap} = Thr_{Input} \times \vartheta \\ Thr_{rot} = Thr_{Input} \times (1 - \vartheta) \end{cases}$$

in which Thr_{Input} represents the total PWM duty cycle percentage of the electronic speed controller before being distributed by the Hybrid Ratio. The Hybrid Ratio, ranging from 0 to 1, allows the system to transition between different operational modes: pure active rotation (no active flapping, $\vartheta = 0$), a hybrid of active rotation and active flapping ($\vartheta \in [0, 1]$), and pure flapping (with passive rotation, $\vartheta = 1$). This ϑ parameter forms the foundation for studying the optimal combination of rotation and flapping to maximise efficiency.

The Hybrid Ratio effectively quantifies the degree of blending between rotational and flapping motions. By further combining Eqs. (17) and (19), the relationship between Thr_{Input} and P_{total} can be derived as follows:

$$\textbf{(20)} \qquad A \cdot Thr_{Input}^2 + B \cdot Thr_{Input} + C = 0$$

in which

$$\textbf{(21)} \qquad \begin{cases} A = 0.002481 \times (1 + 2\vartheta^2 - 2\vartheta) \\ B = 0.03006 \\ C = 0.18188 - P_{total} \end{cases}$$

Further, solving the quadratic equation yields:

$$\textbf{(22)} \qquad Thr_{Input} = \max\left(\frac{-B \pm \sqrt{B^2 - 4AC}}{2A}\right)$$

Given a specified P_{total} and ϑ, Thr_{Input} can be solved using Eq. (22). Once Thr_{Input} is obtained, it can be distributed between the two motors according to Eq. (19). The result from Eq. (22) requires selecting the maximum value because the throttle input Thr_{Input} must be non-negative. Hence, the process in Figure 3 can be implemented to explore the optimal ϑ yielding the highest lift coefficient output under a fixed input power P_{total}. The derived ϑ corresponds to the maximum C_z defines the optimal efficiency point. When $\vartheta = 0$, the rotor operates in pure rotorcraft mode, allowing a direct comparison between the efficiency of pure rotorcraft mode and the optimal efficiency of the Hybrid FWR.

4.4 Lift Coefficient Evaluation Model

This subsection will build a lift coefficient evaluation model that accounts for the asymmetry between the upstroke and downstroke phases. This asymmetry significantly influences the calculation of the cycle-averaged lift coefficient $\overline{C_Z}$, which directly impacts the actual aerodynamic performance in flight. However, the lift coefficient C_z varies continuously during the upstroke and downstroke due to persistent changes in the angle of attack (AoA), as shown in Figure 11. Moreover, Figure 13 highlights that the durations of the upstroke and downstroke cycles vary under different flapping conditions, which further affects the $\overline{C_Z}$ computation. Therefore, $\overline{C_Z}$ is defined in Eq. (23), after accounting for these factors.

$$\textbf{(23)} \qquad \overline{C_Z} = \mu \frac{\sum_{i=0}^{n} C_{Z,up}}{n} + (1 - \mu) \frac{\sum_{i=0}^{n} C_{Z,down}}{n}$$

in which μ is used as a weighting factor to determine the contribution to $\overline{C_Z}$ during the upstroke and downstroke. n represents the number of sampling points used within each stroke phase.

To calculate μ, the total aerodynamic force during the upstroke must first be evaluated. In this study, the total aerodynamic force is simplified using the parameter $\overline{C_{f,up}}$, which is defined as the sum of the average lift coefficient $\left|\frac{\sum_{i=0}^{n} C_{Z,up}}{n}\right|$ and the average drag coefficient $\left|\frac{\sum_{i=0}^{n} C_{X,up}}{n}\right|$ during the upstroke, expressed as:

$$\textbf{(24)} \qquad \overline{C_{f,up}} = \left|\frac{\sum_{i=0}^{n} C_{Z,up}}{n}\right| + \left|\frac{\sum_{i=0}^{n} C_{X,up}}{n}\right|$$

Afterwards, μ is derived as below,

$$\textbf{(25)} \qquad \mu = 0.65 \times \frac{\overline{C_{f,up}} - \overline{C_{f,up,min}}}{\overline{C_{f,up,max}} - \overline{C_{f,up,min}}}$$

in which a normalizing factor is introduced for $\overline{C_{f,up}}$ with regard to its maximum and minimum values $\overline{C_{f,up,max}}$ and $\overline{C_{f,up,min}}$, respectively, Moreover, an empirical factor of 0.65 is included based on high-speed camera experimental results. This μ value varies according to the aerodynamic forces acting on the wing during the upstroke. When $C_{f,up}$ is small, the upstroke time proportion μ is reduced. Conversely, when $C_{f,up}$ is large, μ increases, accurately reflecting the relationship between aerodynamic forces and the upstroke duration.

After completing the formulation of Eqs. (23)– (25), along with the implementation of the lift efficiency evaluation process in Figure 3, we can proceed to analyse the effect of varying ϑ values ranging from 0 to 1 on $\overline{C_Z}$ under a given constant power P_{total}. This allows for identifying a typical value ϑ at which the fixed P_{total} produces the maximum lift coefficient, representing the potential optimal efficiency point for the Hybrid FWR system. The details are elaborated in the next section.

5. OPTIMAL HYBRID RATIO ANALYSIS

5.1 Optimal Condition Predicted by the Developed Model

Figure 16 shows the results generated from the developed model in the previous section, between the Hybrid Ratio ϑ and the cycle-averaged lift coefficient $\overline{C_Z}$ under a steady rotor with constant flapping frequency and rotational speed for power inputs P_{total} ranging from 10W to 30W, with 5W increments. It is evident that the rotor consistently achieves the highest efficiency when ϑ lies between 0.7 and 0.8. Notably, this efficiency is significantly higher than that observed at $\vartheta = 0$, which corresponds to the conventional rotorcraft mode.

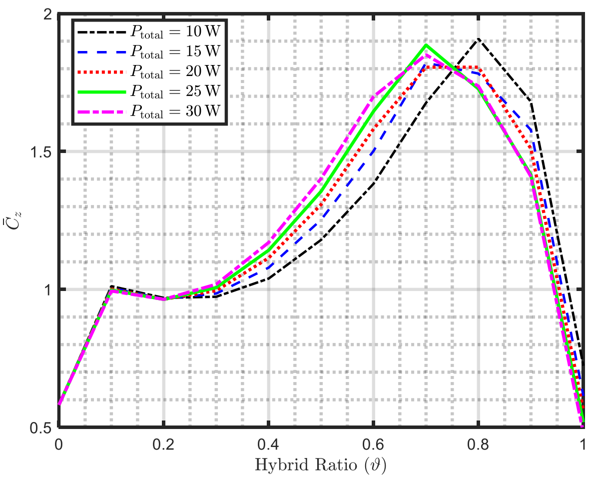

Figure 16: Relationship between $\boldsymbol{\vartheta}$ and $\overline{\boldsymbol{C_Z}}$ w.r.t various defined power settings

The case of $P_{total} = 15W$ in Figure 16 was selected to illustrate the reason behind the existence of the optimal efficiency point. Figure 17 shows its variations of μ, the average lift coefficient, and the average drag coefficient as ϑ ranging from 0 to 1.

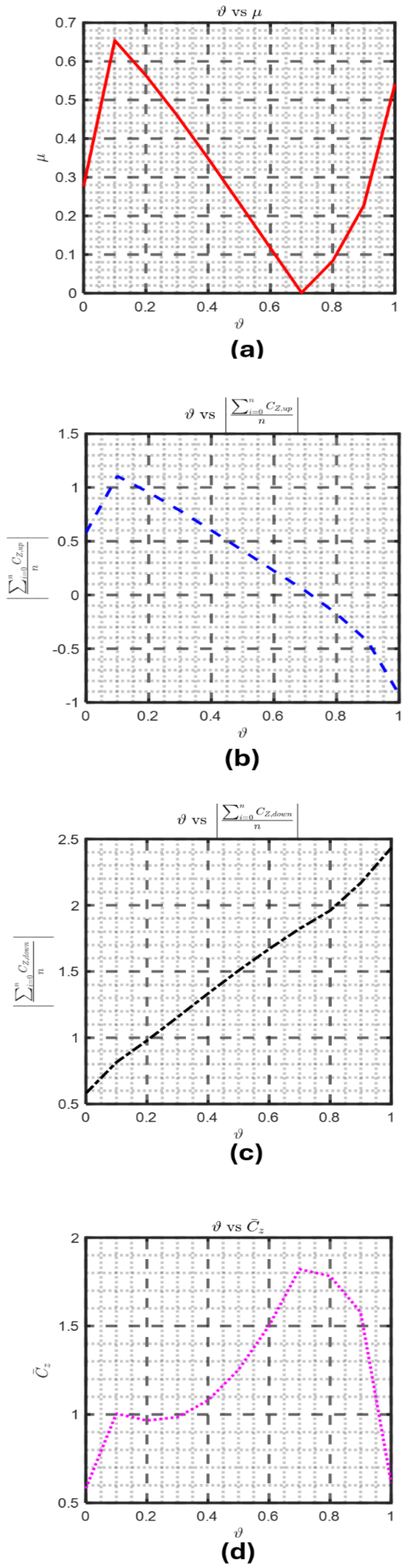

Figure 17: Aerodynamic parameters ($\vartheta = 0\ to\ 1$) when $P_{total} = 15W$

Figure 17(d) indicates that the highest efficiency points of $\overline{C_Z}$ locating at ϑ = 0.7 for the case of $P_{total} = 15W$ This coincides with the point where the upstroke time proportion μ reaches its minimum in Figure 17(a). The same conclusion applies to other P_{total} values as well, but they are omitted here for simplicity.

5.2 Physical Mechanism Governing the Observed Optimal Lift Coefficient

A detailed analysis was carried out in this Subsection to investigate the physical mechanism underlying the relationship between μ and the optimal lift coefficient, focusing on variations in the average lift and drag coefficients during the upstroke ($\overline{C_{Z,up}}$ and $\overline{C_{x,up}}$) and downstroke ($\overline{C_{Z,down}}$ and $\overline{C_{x,down}}$) over a single flapping cycle. The relationship between φ and β_* at different ϑ values for $P_{total} = 15W$ is plotted in Figure 18:

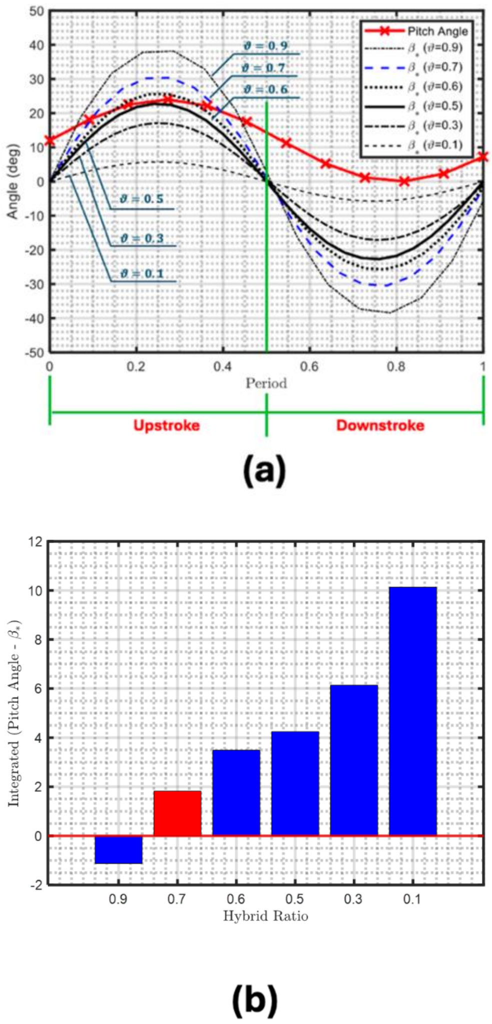

Figure 18: The relationship between φ and β_* under different ϑ values

As observed in Figure 18(a), the β_* curves at $\vartheta = 0.6$ and $\vartheta = 0.7$ appear significantly closer to the pitch angle curve during the upstroke compared to other values of ϑ. To quantitatively assess which of these two cases better approximates the pitch angle curve, the difference between the pitch angle and β_* during the upstroke was computed using Eq. (2), and the resulting effective angle of attack was integrated over time. This evaluation is presented in Figure 18(b).

As shown in the positive region of the vertical axis in Figure 18(b), the integrated value of the effective angle of attack is smallest for $\vartheta = 0.7$, suggesting the closest alignment between β_* and the pitch angle curve. Although $\vartheta = 0.9$ exhibits a similarly small integrated value in the negative region, this corresponds to a negative effective angle of attack, which induces detrimental negative lift during the upstroke and reduces overall aerodynamic efficiency. Disregarding such performance-degrading conditions, it becomes evident that $\vartheta = 0.7$ produces the best match between β_* and the pitch angle during the upstroke. This implies that, under $\vartheta = 0.7$, the aerodynamic forces acting on the wing during the upstroke are minimal, resulting in a reduced $\overline{C_{f,up}}$ as per Eq. (24). Consequently, the upstroke time proportion μ becomes very small according to Eq. (25), indicating that the upstroke phase terminates earlier at $\vartheta = 0.7$ compared to other hybrid ratios.

During the downstroke, the increased W_z in Eq. (1), driven by the higher downstroke velocity, results in a larger $\dot{\beta}$. According to Eq. (2), this indicates a significantly greater effective angle of attack during the downstroke. Consequently, a substantially increased aerodynamic force acts on the wing during this phase, causing the downstroke to occupy a larger fraction of the overall flapping cycle.

Figure 19 shows the average lift and drag coefficients, the magnitude of the average inflow velocity vectors $\overline{\boldsymbol{V}}$, as well as their position and direction during the upstroke and downstroke phases under different hybrid ratio conditions at $P_{total} = 15W$. This diagram essentially duplicates the workflow presented in Figure 3.

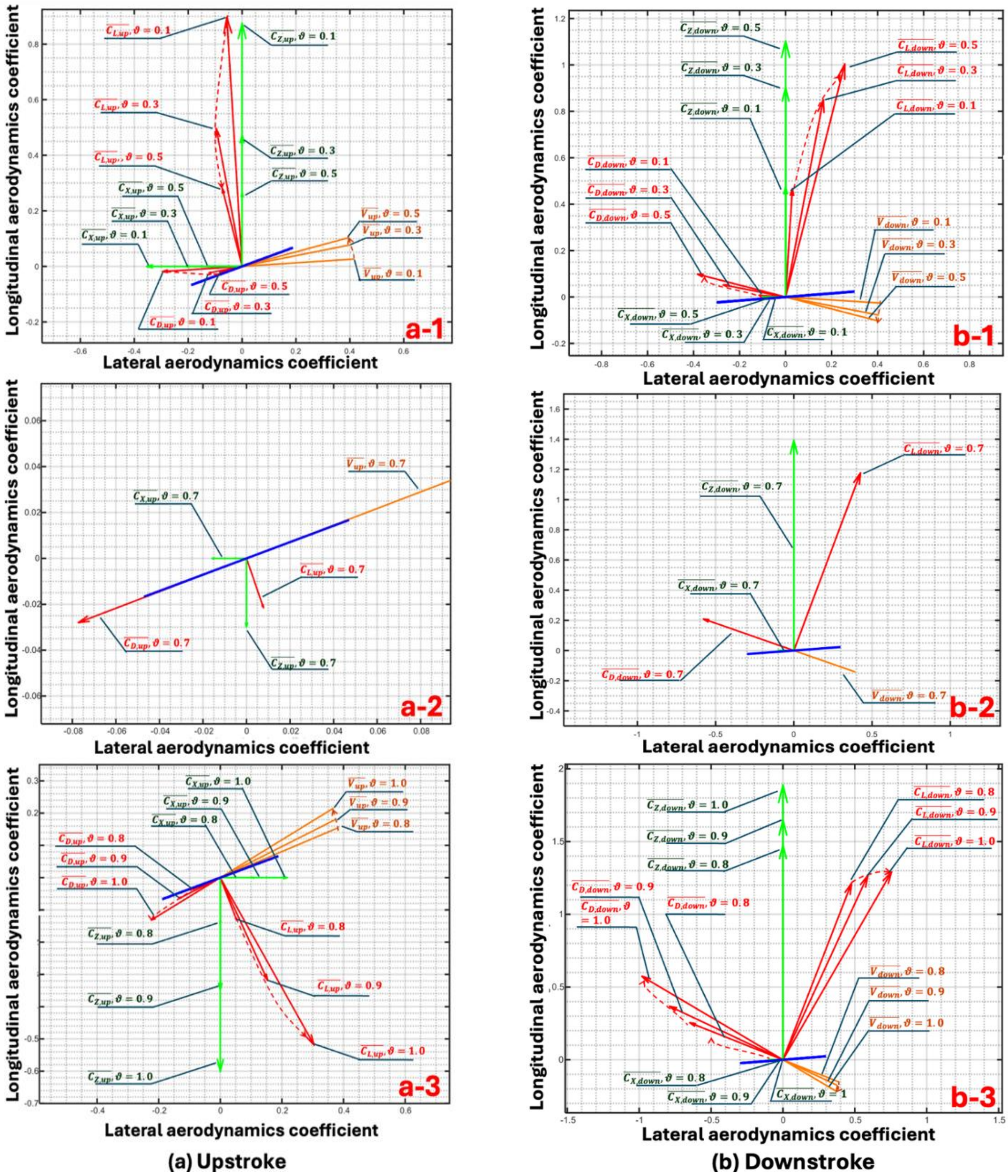

Figure 19: Variation of average aerodynamic coefficients and incoming flow $\overline{V}$, under different ϑ values

Figure 19 explains why the rotor achieves its highest lift coefficient at $\vartheta = 0.7$. Figure 19(a_1, b_1) represents conditions for $\vartheta = 0.1 - 0.6$, Figure 19(a_2, b_2) illustrates the case at $\vartheta = 0.7$, and Figure 19(a_3, b_3) depicts conditions for $\vartheta = 0.8 - 1$. Starting with the upstroke phase analysis (Figure 19*a*), at $\vartheta = 0.7$ (Figure 19a_2), the wing experiences minimal lift and drag coefficients. This aligns with findings from Figure 18, where the effective AoA (α^*) reaches its minimum at this hybrid ratio, resulting in reduced aerodynamic forces. For ϑ (Figure 19a_1), significant positive lift is generated, but substantial drag is also present. Conversely, at $\vartheta = 0.8 - 1$ (Figure 19a_3), the resultant flow strikes the wing's upper surface at an unfavourable angle, causing negative lift and markedly decreasing efficiency. Except at $\vartheta = 0.7$, significant aerodynamic forces during the upstroke result in higher values of μ, consistent with observations from Figure 17*a*.

Figure 19*b* illustrates the average aerodynamic coefficients during the downstroke. Here, the large induced velocity component W_Z creates a significant β_*, substantially increasing the effective angle of attack according to Eqs. (1) and (2). Consequently, notably higher lift $\overline{C_{L,down}}$ and $\overline{C_{D,down}}$ coefficients emerge.

Transformed into the $x_{bl} - z_{bl}$ axes using Eq. (15), these coefficients yield an exceptionally high $\overline{C_{Z,down}}$ that increases with the hybrid ratio. The resultant drag coefficient $\overline{C_{X,down}}$remains relatively low, demonstrating that the large AoA caused by the increased W_Z velocity can significantly enhance the overall lift coefficient of the wing while reducing the drag coefficient.

These combined effects identify $\vartheta = 0.7$ as the optimal efficiency point for $P_{total} = 15W$. At this hybrid ratio, minimal aerodynamic forces during the upstroke significantly reduce the value of μ, thus allocating a greater portion of the cycle to the downstroke. Combined with the substantial lift generated during the downstroke, this extended duration notably increases the cycle-averaged lift coefficient ($\overline{C_Z}$). Although higher hybrid ratios ($\vartheta > 0.7$) generate greater downstroke lift, they also produce negative lift during the prolonged upstroke phase, reducing overall lift. Conversely, at lower hybrid ratios ($\vartheta < 0.7$), although the upstroke lift remains positive, the downstroke lift coefficient is lower, resulting in a reduced overall lift compared to $\vartheta = 0.7$.

The Hybrid FWR achieves superior lift efficiency due to minimised aerodynamic forces during the upstroke, shortening its duration and allowing more time for the downstroke. The significant effective angle of attack during the downstroke enhances lift generation beyond that achievable by conventional micro rotorcraft rotors ($\vartheta = 0$), resulting in superior overall lift performance ($\overline{C_Z}$)

6. EXPERIMENTAL VALIDATION

The experimental setup in Figure 20 was employed to validate the high-lift mechanism of the Hybrid FWR discussed in Section 4. More than 200 experimental trials were conducted to assess its aerodynamic efficiency.

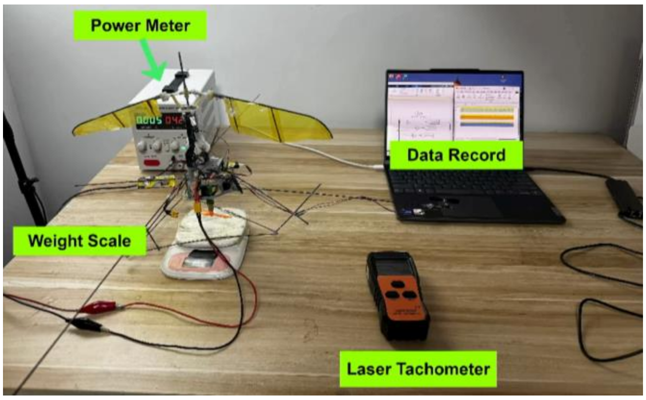

Figure 20: Equipment Testbed built to validate Hybrid FWR efficiency

The setup includes a weight scale, equipped with the Hybrid FWR hardware introduced in Section 2, securely mounted to the table to measure the average lift ($\bar{L}$). A power meter records voltage and current (power) consumption during the rotor's operation. A data acquisition computer transmits precise control commands for Hybrid Ratio and input throttle (Thr_{input}) to the Hybrid FWR flight controller, enabling motor operations that correspond to the desired hybrid ratio. A laser tachometer measures rotor speed by detecting a reflective marker placed on the rotor blade. These tachometer measurements, combined with the flapping frequency captured by a high-speed camera, facilitate validation of the rotor's combined flapping and rotational dynamics.

Once the experimental setup was complete, tests were conducted. To capture the performance data across the entire operating envelope of the Hybrid FWR, experiments were performed for various combinations of $P_{total} = 0 - 20W$ and $\vartheta = 0 - 1$, measuring the resulting lift. Following data collection, rather than directly plotting lift against different hybrid ratios at a constant power level as shown previously in Figure 16, a more practical approach, reflective of typical UAV efficiency assessments, was implemented. Specifically, for predefined constant lift values (30g, 35g, and 40g), the total power consumption was recorded across varying hybrid ratios. The rotor's power efficiency (P_{total}) was then calculated using the following equation:

$$\varepsilon(\text{g/W}) = \frac{\bar{L}}{P_{total}} \tag{26}$$

If the theoretical framework presented in Section 4 is valid, comparing the power efficiency (ε) across various hybrid ratios at a given constant lift ($\bar{L}$) should produce results consistent with those depicted in Figure 16. A summary of the experimental findings is provided in the figure below:

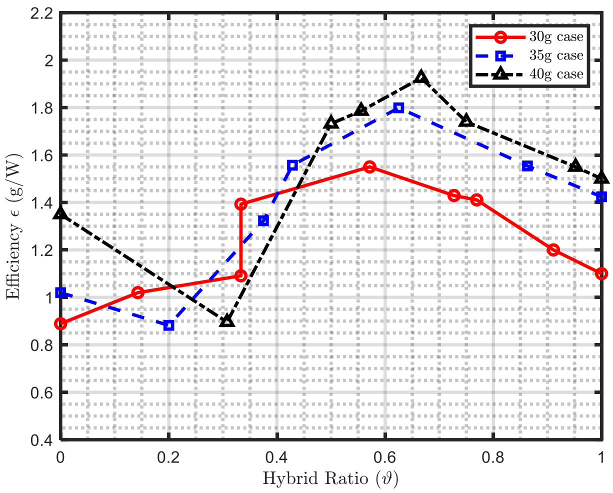

Figure 21: Relationship between Power Efficiency $\varepsilon(\mathrm{g/W})$& Hybrid Ratio $\boldsymbol{\vartheta}$

It can be observed from Figure 21 that at $\vartheta = 0.5 - 0.7$, the power efficiency across various lift conditions reaches its peak. Furthermore, the shape and trend of the efficiency curves closely resemble the theoretical predictions in Figure 16, confirming the validity of the high-lift mechanism proposed in Section 4. Moreover, these experimental results show that the optimal efficiency point occurs at $\vartheta = 0.5 - 0.7$, which is slightly smaller than the theoretical prediction of $\vartheta = 0.7 - 0.8$ in Figure 16. Additionally, the curves there exhibit a trend of continuing to shift with increasing hybrid ratio, which was less pronounced in the theoretical predictions. This discrepancy is likely due to the simplifications in the aerodynamics model, which did not account for certain nonlinear aerodynamic phenomena associated with flapping wings[40], such as the Weis-Fogh effect [41], delayed stall [42,43], and the Kármán vortex street [44] Moreover, the model also did not consider chordwise deformations, aeroelastic effects [45], and resonance phenomena caused by the flexible wing and its structural design, which could influence aerodynamic forces and the upstroke-to-downstroke time proportion μ.

Despite these limitations, the experimental results robustly support the existence of the optimal high-lift coefficient point described in Section 4, along with the mechanism and trends leading to its occurrence. The results further demonstrate that when the Hybrid FWR operates at its optimal efficiency point ($\vartheta = 0.5 - 0.7$), its power efficiency surpasses that of traditional micro rotorcraft rotors ($\vartheta = 0.$) by a factor of up to 2.148 (in the 40g case) and at least 1.743 (in the 30g case), showcasing exceptional performance far beyond that of conventional rotors.

7. CONCLUSIONS

This study presents a novel Hybrid Flapping Wing Rotor (Hybrid FWR) designed to enhance rotor efficiency significantly for micro aerial vehicles (MAVs). By integrating bio-inspired flapping mechanisms with conventional rotorcraft rotation, the proposed system demonstrates substantial performance improvements. Key conclusions include:

- The Hybrid FWR achieved up to a 2.148-fold increase in power efficiency compared to traditional rotors.
- A comprehensive mathematical model was developed to predict the aerodynamic performance of the Hybrid FWR.
- The mathematical model successfully predicted an optimal hybrid ratio value of approximately 0.7, effectively reducing aerodynamic resistance during the upstroke and enhancing lift during the downstroke.
- Experimental validations consistently supported theoretical predictions, confirming the reliability of the developed aerodynamic model and the theoretical high-lift mechanism and establishing the hybrid ratio $\vartheta = 0.5 - 0.7$ as the optimal operational point.

These findings represent significant advancements for the MAV sector, addressing core challenges such as limited endurance and operational efficiency. By leveraging bio-inspired mechanisms, this approach can substantially enhance MAV flight performance.

Future research directions should emphasize refining control systems and structural designs to ensure the practical applicability of Hybrid FWRs. Translating the demonstrated aerodynamic benefits into operational MAV platforms could expand their usage across various sectors.

8. REFERENCES

1. Berkil, E., “The Diverse Applications of Aerospace Drones: From Defense to Humanitarian and Commercial Uses,” Next Generation Journal for The Young Researchers, Vol. 8, No. 1, 2024, p. 69. https://doi.org/10.62802/6hwvpp26
2. Derricott, J. C., Willis, J. B., Peterson, C. K., Franke, K. W., and Hedengren, J. D., “Disaster Reconnaissance Using Multiple Small Unmanned Aerial Vehicles,” Mechanical Engineering, Vol. 141, No. 06, 2019, pp. S7–S11. https://doi.org/10.1115/1.2019-JUN5
3. Gad-el-Hak, M., “Micro-Air-Vehicles: Can They Be Controlled Better?,” Journal of Aircraft, Vol. 38, No. 3, 2001, pp. 419–429. https://doi.org/10.2514/2.2807

4. Li, H., Guo, S., Zhang, Y. L., Zhou, C., and Wu, J. H., “Unsteady Aerodynamic and Optimal Kinematic Analysis of a Micro Flapping Wing Rotor,” Aerospace Science and Technology, Vol. 63, 2017, pp. 167–178. https://doi.org/10.1016/j.ast.2016.12.025

5. Liu, Y., Zhang, Y., and Wu, J., “Design and Experimental Study on a Flapping Wing Micro Air Vehicle,”, 2019, pp. 1330–1342. https://doi.org/10.1007/978-981-13-3305-7_106

6. Haider, N., Shahzad, A., Mumtaz Qadri, M. N., and Ali Shah, S. I., “Recent Progress in Flapping Wings for Micro Aerial Vehicle Applications,” Proceedings of the Institution of Mechanical Engineers, Part C: Journal of Mechanical Engineering Science, Vol. 235, No. 2, 2021, pp. 245–264. https://doi.org/10.1177/0954406220917426

7. Chen, C., and Zhang, T., “A Review of Design and Fabrication of the Bionic Flapping Wing Micro Air Vehicles,” Micromachines, Vol. 10, No. 2, 2019, p. 144. https://doi.org/10.3390/mi10020144

8. McMichael, J. M., & Francis, M. S. (1997). Micro Air Vehicles: Toward a New Dimension in Flight. Defense Advanced Research Projects Agency.

9. Hwang, I. S., Min, S. Y., Lee, C. H., and Kim, S. J., “Development of a Four-Rotor Cyclocopter,” Journal of Aircraft, Vol. 45, No. 6, 2008, pp. 2151–2157. https://doi.org/10.2514/1.35575

10. Talbot, P. D., Phillips, J. D., and Totah, J. J., “Selected Design Issues of Some High-Speed Rotorcraft Concepts,” Journal of Aircraft, Vol. 30, No. 6, 1993, pp. 864–871. https://doi.org/10.2514/3.46428

11. Serré, R., Fournier, H., and Moschetta, J.-M., “A Design Methodology for Quiet and Long Endurance MAV Rotors,” International Journal of Micro Air Vehicles, Vol. 11, 2019. https://doi.org/10.1177/1756829319845937

12. Paulos, J., & Yim, M. (2015, May). Flight performance of a swashplateless micro air vehicle. In 2015 IEEE International Conference on Robotics and Automation (ICRA) (pp. 5284-5289). IEEE. https://doi.org/10.1109/ICRA.2015.7139936

13. Prothin, S., and Doué, N., “Design and Analysis of a Thrust-Vectoring Coaxial-Rotor Micro Air Vehicle,”, 2015. https://doi.org/10.4050/F-0071-2015-10292

14. Bhatnagar, K., Bansal, D., Arya, B., and Abhishek, A., “Design and Development of Swashplateless Micro Helicopter with Pitch-Lag Coupling,”, 2024. https://doi.org/10.4050/F-0080-2024-1291

15. Phan, H. V., Truong, Q. T., Au, T. K. L., and Park, H. C., “Effect of Wing Kinematics Modulation on Aerodynamic Force Generation in Hovering Insect-Mimicking Flapping-Wing Micro Air Vehicle,” Journal of Bionic Engineering, Vol. 12, No. 4, 2015, pp. 539–554. https://doi.org/10.1016/S1672-6529(14)60144-X

16. Phan, H. V., Truong, Q. T., and Park, H. C., “An Experimental Comparative Study of the Efficiency of Twisted and Flat Flapping Wings during Hovering Flight,” Bioinspiration & Biomimetics, Vol. 12, No. 3, 2017, p. 036009. https://doi.org/10.1088/1748-3190/aa65e6

17. Sullivan, D. B., Righi, F., Hartl, D. J., and Rogers, J., “Shape Memory Alloy Rotor Blade Deicing,”, 2013. https://doi.org/10.2514/6.2013-1915

18. Friedman, D. H., Bieniawski, S., and Hartl, D., “Simulation and Control Design for Shape Memory Alloy Torque Tubes,”, 2011. https://doi.org/10.1115/SMASIS2011-5132

19. Jin, F., Zang, C., Xing, G., Ma, Y., Yuan, S., and Jia, Z., “Resonant Peak Reduction of a Rotor System Based on Gradually Variable Stiffness of Supports with Shape Memory Alloy Springs,” Journal of Sound and Vibration, Vol. 591, 2024, p. 118626. https://doi.org/10.1016/j.jsv.2024.118626

20. WEN, Q., GUO, S., LI, H., and DONG, W., “Nonlinear Dynamics of a Flapping Rotary Wing: Modeling and Optimal Wing Kinematic Analysis,” Chinese Journal of Aeronautics, Vol. 31, No. 5, 2018, pp. 1041–1052. https://doi.org/10.1016/j.cja.2018.03.004

21. Ji, B., Zhu, Q., Guo, S., Yang, F., Li, Y., Zhu, Z., Chen, S., Song, R., and Li, Y., “Design and Experiment of a Bionic Flapping Wing Mechanism with Flapping-Twist-Swing Motion Based on a Single Rotation,” AIP Advances, Vol. 10, No. 6, 2020. https://doi.org/10.1063/5.0008792

22. Pan, Y., Guo, S., Whidborne, J., and Huang, X., “Aerodynamic Performance of a Flyable Flapping Wing Rotor with Dragonfly-like Flexible Wings,” Aerospace Science and Technology, Vol. 148, 2024, p. 109090. https://doi.org/10.1016/j.ast.2024.109090

23. Gil-Prieto, D., MacManus, D. G., Zachos, P. K., and Bautista, A., “Assessment Methods for Unsteady Flow Distortion in Aero-Engine Intakes,” Aerospace Science and Technology, Vol. 72,

2018, pp. 292–304. https://doi.org/10.1016/j.ast.2017.10.029

24. Guo, S., Li, H., Zhou, C., Zhang, Y. L., He, Y., and Wu, J. H., "Analysis and Experiment of a Bio-Inspired Flyable Micro Flapping Wing Rotor," Aerospace Science and Technology, Vol. 79, 2018, pp. 506–517. https://doi.org/10.1016/j.ast.2018.06.009

25. Guo, S., Li, D., and Wu, J., "Theoretical and Experimental Study of a Piezoelectric Flapping Wing Rotor for Micro Aerial Vehicle," Aerospace Science and Technology, Vol. 23, No. 1, 2012, pp. 429–438. https://doi.org/10.1016/j.ast.2011.10.002

26. Lietz, C., Schaber, C. F., Gorb, S. N., and Rajabi, H., "The Damping and Structural Properties of Dragonfly and Damselfly Wings during Dynamic Movement," Communications Biology, Vol. 4, No. 1, 2021, p. 737. https://doi.org/10.1038/s42003-021-02263-2

27. Wang, Z. J., "Dissecting Insect Flight," Annual Review of Fluid Mechanics, Vol. 37, No. 1, 2005, pp. 183–210. https://doi.org/10.1146/annurev.fluid.36.050802.121940

28. Nakata, T., Liu, H., Tanaka, Y., Nishihashi, N., Wang, X., and Sato, A., "Aerodynamics of a Bio-Inspired Flexible Flapping-Wing Micro Air Vehicle," Bioinspiration & Biomimetics, Vol. 6, No. 4, 2011, p. 045002. https://doi.org/10.1088/1748-3182/6/4/045002

29. Wang, H., Zeng, L., Liu, H., and Yin, C., "Measuring Wing Kinematics, Flight Trajectory and Body Attitude during Forward Flight and Turning Maneuvers in Dragonflies," Journal of Experimental Biology, Vol. 206, No. 4, 2003, pp. 745–757. https://doi.org/10.1242/jeb.00183

30. Truong, Q. T., Nguyen, Q. V., Truong, V. T., Park, H. C., Byun, D. Y., and Goo, N. S., "A Modified Blade Element Theory for Estimation of Forces Generated by a Beetle-Mimicking Flapping Wing System," Bioinspiration & Biomimetics, Vol. 6, No. 3, 2011, p. 036008. https://doi.org/10.1088/1748-3182/6/3/036008

31. Li, H., and Guo, S., "Aerodynamic Efficiency of a Bioinspired Flapping Wing Rotor at Low Reynolds Number," Royal Society Open Science, Vol. 5, No. 3, 2018, p. 171307. https://doi.org/10.1098/rsos.171307

32. Wan, J., and Pavel, M. D., "Designing the Ornicopter, a Tailless Helicopter with Active Flapping Blades: A Case Study," Proceedings of the Institution of Mechanical Engineers, Part G: Journal of Aerospace Engineering, Vol. 230, No. 12, 2016, pp. 2195–2219. https://doi.org/10.1177/0954410015622228

33. Deng, S., Percin, M., van Oudheusden, B., Remes, B., and Bijl, H., "Experimental Investigation on the Aerodynamics of a Bio-Inspired Flexible Flapping Wing Micro Air Vehicle," International Journal of Micro Air Vehicles, Vol. 6, No. 2, 2014, pp. 105–115. https://doi.org/10.1260/1756-8293.6.2.105

34. Lee, Y. J., Lua, K. B., Lim, T. T., and Yeo, K. S., "Corrigendum: A Quasi-Steady Aerodynamic Model for Flapping Flight with Improved Adaptability (2016 Bioinsp. Biomim. 11 036005)," Bioinspiration & Biomimetics, Vol. 11, No. 4, 2016, p. 049501. https://doi.org/10.1088/1748-3190/11/4/049501

35. Rylko, A., Di Milano, P., Van't Hoff, S., and Padfield, G., "Rotorcraft Flight Simulation to Support Aircraft Certification: A Review of the State of the Art with an Eye to Future Applications."

36. Lu, L., Agarwal, D., Padfield, G. D., White, M. D., and Cameron, N., "A New Heuristic Approach to Rotorcraft System Identification," Journal of the American Helicopter Society, Vol. 68, No. 2, 2023, pp. 42–58. https://doi.org/10.4050/JAHS.68.022005

37. Padfield, G. D., Pavel, M. D., Casolaro, D., Roth, G., Hamers, G., & Taghizad, A. (2005, June). Simulation fidelity of real-time helicopter simulation models. In 61st Annual Forum of the American Helicopter Society.

38. Huang, X., Lu, L., Whidborne, J. F., & Guo, S. (2023). Modelling and simulation of a novel bio-inspired flapping-wing rotary MAV.

39. Kumar, G. C. V., and Juliyana, M. R., "Design and Analysis of Flapping Wing," Applied Mechanics and Materials, Vols. 110–116, 2011, pp. 3495–3499. https://doi.org/10.4028/www.scientific.net/AMM.110-116.3495

40. KOLOMENSKIY, D., MOFFATT, H. K., FARGE, M., and SCHNEIDER, K., "The Lighthill–Weis-Fogh Clap–Fling–Sweep Mechanism Revisited," Journal of Fluid Mechanics, Vol. 676, 2011, pp. 572–606. https://doi.org/10.1017/jfm.2011.83

41. Usab, W. J., Hardin, J., and Bilanin, A. J., "Bio-inspired Delayed Stall Propulsor," IEEE Journal of Oceanic Engineering, Vol. 29, No. 3, 2004, pp. 756–765. https://doi.org/10.1109/JOE.2004.833112

42. Sudhakar, Y., and Vengadesan, S., "The Functional Significance of Delayed Stall in Insect

Flight," Numerical Heat Transfer, Part A: Applications, Vol. 58, No. 1, 2010, pp. 65–83. https://doi.org/10.1080/10407782.2010.490453

43. Thoraval, M.-J., Takehara, K., Etoh, T. G., Popinet, S., Ray, P., Josserand, C., Zaleski, S., and Thoroddsen, S. T., "Von Kármán Vortex Street within an Impacting Drop," Physical Review Letters, Vol. 108, No. 26, 2012, p. 264506. https://doi.org/10.1103/PhysRevLett.108.264506

44. Chen, S., Li, H., Guo, S., Tong, M., and Ji, B., "Unsteady Aerodynamic Model of Flexible Flapping Wing," Aerospace Science and Technology, Vol. 80, 2018, pp. 354–367. https://doi.org/10.1016/j.ast.2018.07.017

45. Shyy, W., Aono, H., Chimakurthi, S. K., Trizila, P., Kang, C.-K., Cesnik, C. E. S., and Liu, H., "Recent Progress in Flapping Wing Aerodynamics and Aeroelasticity," Progress in Aerospace Sciences, Vol. 46, No. 7, 2010, pp. 284–327. https://doi.org/10.1016/j.paerosci.2010.01.001